Seasonal variations of the electron density distribution in the polar region during geomagnetically quiet periods near solar maximum

N. Kitamura,[1] A. Shinbori,[2] Y. Nishimura,[1] T. Ono,[1] M. Iizima,[1,3] and A. Kumamoto[1,4]

Received 8 April 2008; revised 8 July 2008; accepted 9 September 2008; published 14 January 2009.

[1] Meridional electron density distributions above 45° invariant latitude (ILAT) during geomagnetically quiet periods are statistically studied. Electron density data were obtained from plasma waves observed by the Akebono satellite from March 1989 to February 1991 (near solar maximum) in an altitude range of 274–10,500 km. Field-aligned electron density profiles were fitted by the sum of exponential and power law functions. The transition height, where the power law term equals the exponential term, is highest in the summer (at low solar zenith angle (SZA)) at ~4000 km and lowest in the winter (at high SZA) at ~1800 km in a region of ILAT $\geq$ 70°; this is caused by the larger scale height in the summer (~550 km) than that in the winter (~250 km). The largest seasonal variation and SZA dependence of the electron density are found at an altitude of ~2000 km with a factor of ~50 (~10^4 /cc in the summer, ~10^3 /cc in the winter) in the trough, auroral, and polar cap regions. The seasonal variation and SZA dependence are smaller, about a factor of 5–10, above ~5000 km. Day-night asymmetries in each season (within a factor of 5) are smaller than the seasonal variation. The scale height is larger in the dayside than in the nightside in each season. These results indicate that photoionization processes in the ionosphere strongly control electron density distributions up to at least ~5000 km in the trough, auroral, and polar cap regions.

Citation: Kitamura, N., A. Shinbori, Y. Nishimura, T. Ono, M. Iizima, and A. Kumamoto (2009), Seasonal variations of the electron density distribution in the polar region during geomagnetically quiet periods near solar maximum, *J. Geophys. Res.*, *114*, A01206, doi:10.1029/2008JA013288.

1. Introduction

[2] The electron density in the polar region is one of the most important parameters in the study of acceleration of outflowing ions and plasma supply processes toward the magnetosphere. The ambient electron density affects the properties of Alfvén waves carrying field-aligned currents and plasma waves in the polar region [*Fukunishi et al.*, 1991; *Lysak and Lotko*, 1996; *Schreiber et al.*, 2002; *Xiao et al.*, 2007]. In addition, it is suggested that the ambient electron density controls auroral acceleration and auroral kilometric radiation (AKR) [*Kumamoto et al.*, 2001, 2003; *Morooka and Mukai*, 2003; *Green et al.*, 2004]. The field lines in the polar cap region are opened toward the interplanetary medium, while the field lines in the plasmasphere and trough region are connected to the other hemisphere. In the polar cap, the plasma supplied from the ionosphere, where the electron density is controlled by photochemical processes, can escape into the magnetotail as the polar wind [*Ganguli*, 1996; *Yau and André*, 1997; *Yau et al.*, 2007] and cleft ion fountain [*Lockwood et al.*, 1985a, 1985b; *Moore et al.*, 1986; *Pollock et al.*, 1990], in contrast to the closed field lines in the plasmasphere and trough region.

[3] The electron density distribution at low (<3000 km) and high (>4000 km) altitudes in the polar region has been examined separately. Below an altitude of 3000 km, the distribution has been considered as an extension of the ionosphere, based on in situ [e.g., *Grebowsky et al.*, 1990] and sounder [e.g., *Nelms and Lockwood*, 1967; *Matuura and Ondoh*, 1969; *Persoon et al.*, 1983] observations. At high altitudes, *Persoon et al.* [1983] developed an empirical model of electron densities for a geocentric distance (r) between 2.0 and 4.66 R_E, using the maximum frequency of whistler mode waves observed by the Dynamics Explorer 1 (DE-1) satellite in a region of invariant latitudes (ILAT) higher than 71.6°. They proposed a field-aligned electron density profile under the condition in which photochemical processes could be neglected. Assuming a single ion composition, the continuity equation gives $N_e u/B$ = const., where N_e, u, and B are the electron density, upward plasma velocity, and magnetic field strength, respectively. Since B is proportional to r^{-3} in a dipole field, if u is constant, N_e decreases in proportion to r^{-3}. It was identified that $N_e \propto r^{-3.85}$, which implied that u increased approximately linearly with r [*Persoon et al.*, 1983]. *Hilgers* [1992] and *Nsumei et al.* [2003] derived the power index of about −5 based on Langmuir probe observations by the Viking satellite and

[1]Department of Geophysics, Tohoku University, Sendai, Japan.
[2]Solar-Terrestrial Environment Laboratory, Nagoya University, Nagoya, Japan.
[3]Now at Shukutoku Gakuen, Tokyo, Japan.
[4]Now at Planetary Plasma and Atmospheric Research Center, Tohoku University, Sendai, Japan.

0148-0227/09/2008JA013288

sounder observations by the IMAGE satellite, indicating a stronger acceleration ($u \propto r^2$).

[4] From a comparison of electron density profiles between high (2.0–4.66 R_E) and low (1.16–1.55 R_E) altitudes in the polar region, *Persoon et al.* [1983] indicated existence of a transition of the electron density profile between 1.55 and 2.0 R_E. *Kletzing et al.* [1998] demonstrated that the electron density profile including the transition altitude could be explained by the sum of an exponential function for an altitude of below about 3000 km and a height-dependent power law function for an altitude of above about 3000 km based on Langmuir probe observations by the S3–3 satellite. However, the lack of observations, especially in an altitude range of 1000–4000 km, has made it difficult to clarify the unified electron density distribution model connecting the ionospheric altitude to the distant region above 2 R_E.

[5] The electron density in the polar region has a large seasonal variation. Below an altitude of 1000 km, the electron density in the summer was 2–10 times larger than that in the winter [e.g., *Nishida*, 1967; *Grebowsky et al.*, 1990]. In an altitude range of 1000–4000 km, *Chandler et al.* [1991] performed a statistical study of the ion density on the seasonal variation, using the retarding ion mass spectrometer on board DE-1. They showed that the ion density in the winter decreased by about a factor of 3, compared with that in the summer. At an altitude of about 6000 km, *Laakso et al.* [2002] also performed a statistical study on the seasonal variation, using the spacecraft potential measured by the Polar satellite. They showed that the electron density in the summer increased by a factor of 10–100, compared with that in winter. These studies on the seasonal variation of the plasma density are restricted in rather narrow altitude ranges. On the other hand, above 1.75 R_E, there are statistical studies covering a wide altitude range. These studies showed that the seasonal variation and solar zenith angle (SZA) dependence of the electron density are small (a factor of 1–10) above 5 R_E, and the electron density gradient between 1.75 and 5 R_E is steeper in the summer (sunlit) than that in the winter (dark) [*Laakso and Grard*, 2002; *Johnson and Wygant*, 2003; *Nsumei et al.*, 2008]. In order to clarify the unified electron density distribution, it is important to investigate the seasonal variation continuously from ionospheric altitudes to above 2 R_E.

[6] In addition to the seasonal variation, a large day-night asymmetry with a factor of 3–10 [*Nishida*, 1967; *Chan and Colin*, 1969; *Johnson et al.*, 2001] and strong dependence on geomagnetic activities (up to a factor of 100) [*Laakso and Grard*, 2002; *Nsumei et al.*, 2003, 2008; *Tu et al.*, 2004, 2005, 2007] in the polar cap should also be taken into account when investigating the electron density distribution. In the present study, we exclude geomagnetically active periods and construct electron density distribution models for geomagnetically quiet periods.

[7] Investigations of electron density profiles in the polar region have suffered from ambiguities of the plasma density due to difficulties of measurements. Since spacecraft are positively charged in tenuous plasmas except during eclipse periods [*Scudder et al.*, 2000; *Pedersen et al.*, 2008], and ions in the polar region are cold [*Drakou et al.*, 1997], it is very difficult to observe the ion density precisely using particle detectors. Although the in situ electron density can be derived from spacecraft potential measurements, the spacecraft potentials are affected not only by the electron density but also by the plasma temperature and photoelectrons depending on solar activities [*Adrian*, 2002; *Pedersen et al.*, 2008]. In contrast, natural plasma wave observations can derive precise in situ electron densities without spacecraft potential effects. The Akebono satellite provides a large amount of in situ electron density data derived from such natural plasma wave observations. The database allows us to obtain reliable electron density models by considering the seasonal variation and day-night asymmetry in the polar region. Moreover, the Akebono satellite covers an altitude range of 274–10,500 km, which has not been fully investigated in statistical studies.

[8] In the present paper, we derive the meridional electron density distributions (ILAT $\geq$ 45°) in the dayside and nightside in an altitude range of 1000–10,500 km during geomagnetically quiet periods, using 2 years of electron density data derived from natural plasma wave observations by Akebono near solar maximum. We investigate the seasonal variation of the field-aligned and latitudinal electron density distributions in a region of ILAT $\geq$ 45°. We also analyze the SZA dependence of field-aligned electron density profiles in the nightside polar region (ILAT $\geq$ 70°). Finally, the results are compared to the density models which have been proposed.

2. Data Analysis Method

[9] The Akebono satellite was launched on 22 February 1989 with an initial perigee of 274 km, apogee of 10,500 km, and inclination of 75°. The plasma wave and sounder (PWS) experiments were designed to measure AC electric fields in a frequency range from 20 kHz to 5.1 MHz with a time resolution of 2 s [*Oya et al.*, 1990].

[10] The electron density is derived from the same method as that used by *Kumamoto et al.* [2001, 2006] and *Shinbori et al.* [2005]. By using the Akebono PWS data, the in situ electron density is obtained from the upper-hybrid resonance (UHR) frequency (f_{UHR}) or electron plasma frequency (f_{pe}). The electron density is derived from f_{UHR} when f_{pe} is larger than the electron cyclotron frequency (f_{ce}). For the case of f_{pe} smaller than f_{ce}, we calculate the electron density from the maximum frequency of whistler mode waves (=f_{pe}). However, when the maximum frequency of whistler mode waves is not clearly determined, f_{UHR} is used. The electron cyclotron frequency is calculated using the IGRF-10 model. The relation between f_{UHR} and f_{pe} is given by the following equation (1),

$$f_{pe} = \sqrt{f_{UHR}^2 - f_{ce}^2}. \quad (1)$$

According to the following equation (2), the electron density (N_e) is calculated,

$$N_e \approx \left(\frac{f_{pe}}{8.98}\right)^2, \quad (2)$$

where N_e is in /cc and f_{pe} is in kHz. The range of f_{pe} from 20 kHz to 5.1 MHz corresponds to the electron density from 5.5 to 3.2 $\times$ 10^5 /cc. In cases of f_{pe} lower than 20 kHz, the

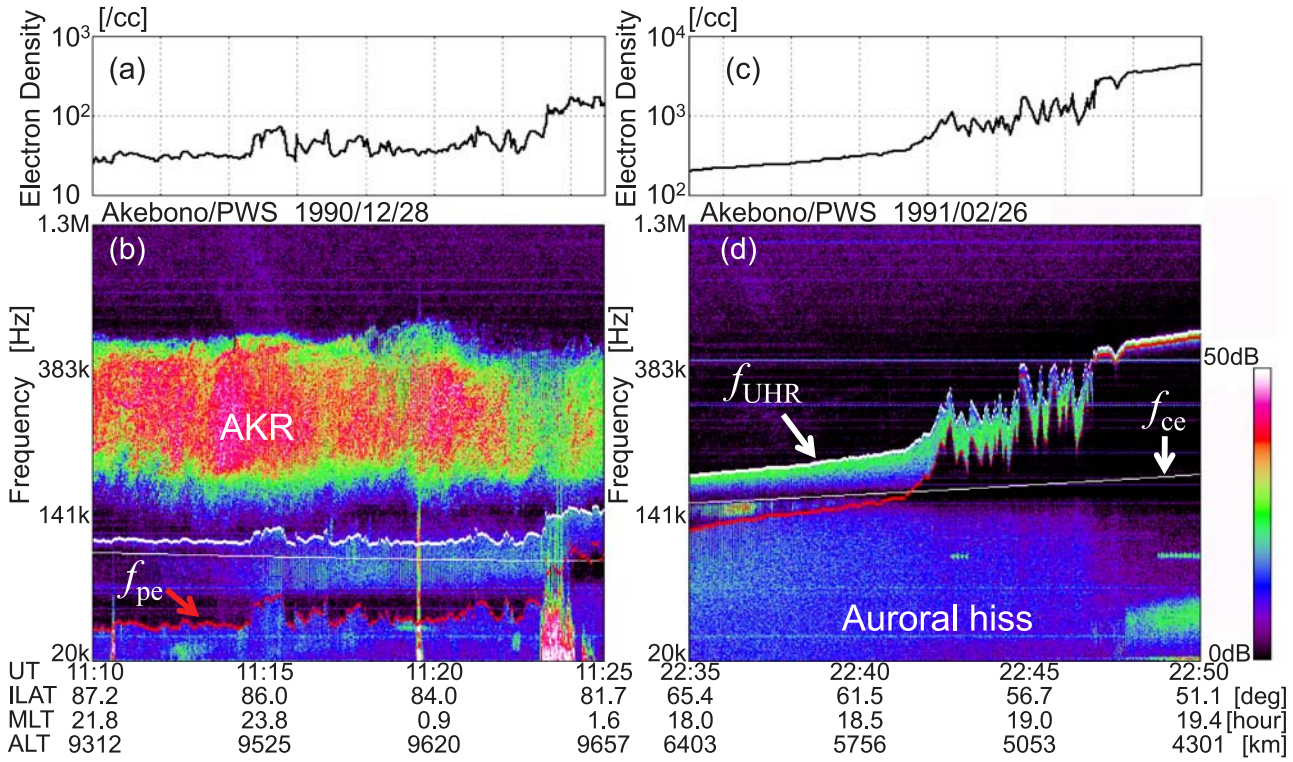

Figure 1. Dynamic spectra of plasma waves observed on (b) 28 December 1990 and (d) 26 February 1991 and (a and c) derived plasma densities. Figures 1b and 1d were observed in the polar cap, and the trough and around the plasmapause, respectively. Here f_{UHR}, f_{ce}, and f_{pe} are shown in the dynamic spectra by thick white, thin white, and red curves, respectively.

electron densities cannot be derived, and the data are regarded as "below 5.5 /cc."

[11] Figures 1b and 1d show examples of the dynamic spectra in a frequency range from 20 kHz to 1.3 MHz observed by PWS on 28 December 1990 and 26 February 1991, respectively. Plasma waves were observed in the polar cap and in the trough and around the plasmapause, respectively. Here f_{UHR}, f_{ce}, and f_{pe} are shown in the dynamic spectra as thick white, thin white, and red curves, respectively. Figures 1a and 1c represent the electron density derived from the dynamic spectra shown in Figures 1b and 1d. The electron densities are obtained from maximum frequencies of whistler mode waves before 1123:04 (Figure 1b) and 2239:30 UT (Figure 1d). After these periods, f_{UHR} is used to calculate the electron density according to equations (1) and (2). As can be seen in Figures 1a and 1c, the densities obtained from the two methods are smoothly connected to each other in each case.

[12] We use the electron density data from March 1989 to February 1991 corresponding to the solar maximum, in the present statistical study. The monthly mean $F_{10.7}$ solar radio flux index in this period ranges between 171 and 240 (Figure 7c). It is reported that the variation of the solar activity affects electron densities [*Johnson and Wygant*, 2003; *Kumamoto et al.*, 2006]. In order to investigate the solar activity dependence, further investigations are required in the future using much more data. The geomagnetically quiet periods are defined as the times when the *SYM-H* index is in a range from −10 to 40 nT and the *Kp* index is less than or equal to 2+ for the preceding 3 h.

[13] In order to investigate a seasonal variation of electron density profiles, the electron density data are classified into the summer, equinox, and winter seasons. The electron density data observed in the northern hemisphere in May, June, and July, and those observed in the southern hemisphere in November, December, and January, are categorized into the summer season. The winter season is defined as vice versa. The other months are defined as the equinox season. The electron density data are sorted into the dayside (0600–1800 magnetic local time (MLT)) and the nightside (1800–2400 and 0000–0600 MLT), and 100 km bins in altitude. Only the electron density data derived in a region of ILAT $\geq 45^\circ$ are used in the present study. The ILAT grid size is 5° except for the "$\geq 80^\circ$" bin. Then, the median is calculated using electron density data derived from all of the individual spectra in each bin. The median is used rather than the average value in order to eliminate the effect of the data "below 5.5 /cc." When less than half of the data in the bin are "below 5.5 /cc," the median is not affected by data "below 5.5 /cc." In the cases where more than half of the data are "below 5.5 /cc," the bin is ignored in obtaining the empirical models.

[14] For each ILAT bin in the dayside and nightside, field-aligned profiles of the median electron density data are fitted by using a nonlinear least squares fitting method with the following model function,

$$N_e = n_1 \exp(-z/h) + n_2 r^{-\alpha}, \quad (3)$$

where z is the altitude from the Earth's surface in km, r is the geocentric distance in R_E, and n_1, h, n_2, and α are

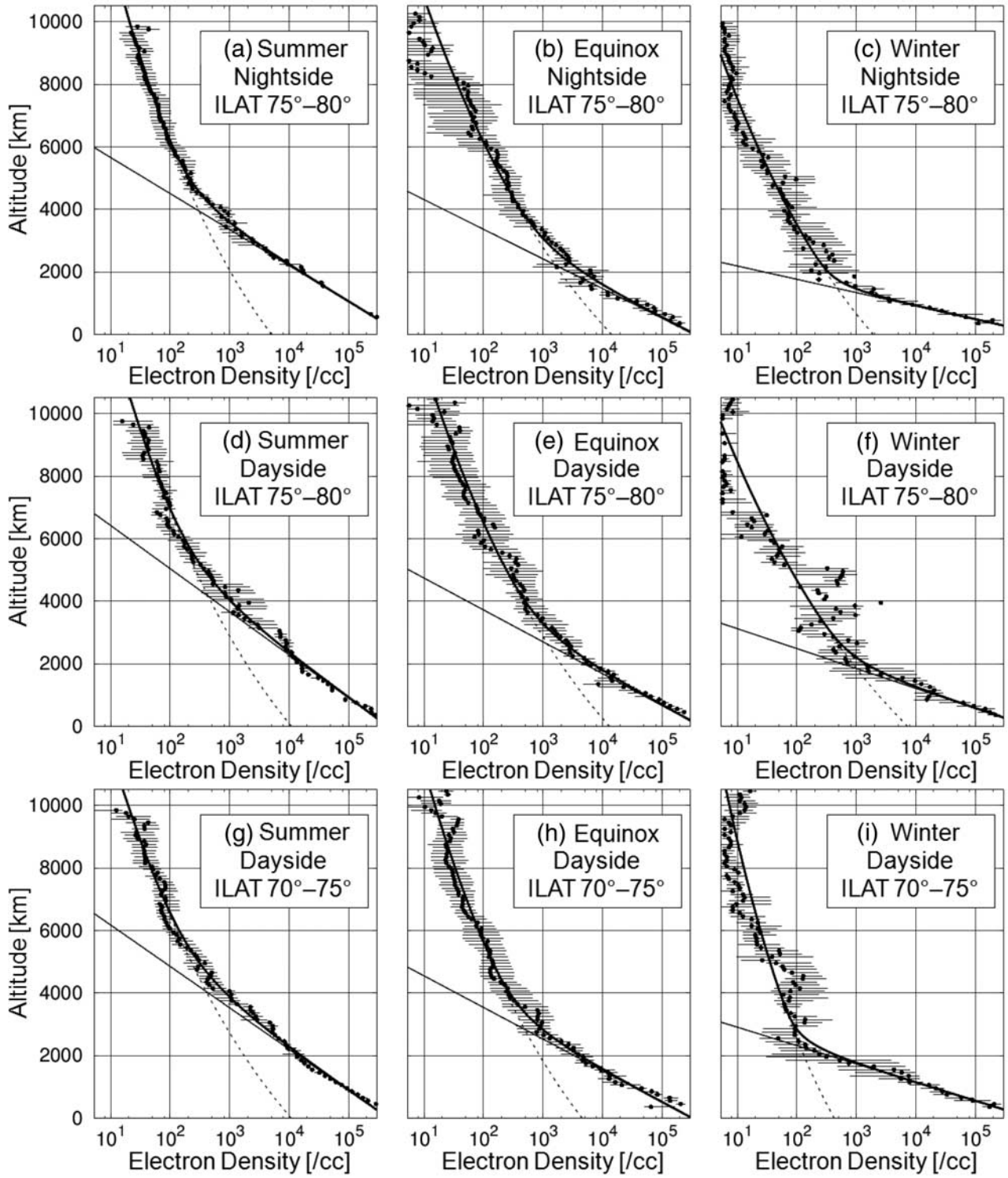

Figure 2. Field-aligned profiles of the electron density (a, b, and c) at 75°–80° ILAT in the nightside, (d, e, and f) at 75°–80° ILAT in the dayside, and (g, h, and i) at 70°–75° ILAT in the dayside. Electron density profiles in each season are shown in Figures 2a, 2d, and 2g (summer); Figures 2b, 2e, and 2h (equinox); and Figures 2c, 2f, and 2i (winter). Thick solid curves show the fitted profiles using equation (3). Dotted curves show the power function term in equation (3). Thin solid lines show the exponential term in equation (3). Solid dots denote median electron densities. Error bars indicate quartiles, which show 25% deviations on either side of the medians.

Table 1. Coefficients, Root-Mean-Square Errors of the Coefficients, and ε in the Summer in the Dayside

Invariant Latitude	$\log_{10}(n_1$ (/cc))	h (km)	$\log_{10}(n_2$ (/cc))	α	ε
45°–50°	5.87 ± 0.09	370 ± 23	4.02 ± 0.06	2.09 ± 0.20	0.075
50°–55°	5.55 ± 0.05	521 ± 22	3.46 ± 0.07	0.78 ± 0.21	0.080
55°–60°	5.71 ± 0.04	486 ± 17	3.42 ± 0.08	1.66 ± 0.24	0.080
60°–65°	5.63 ± 0.04	534 ± 17	3.84 ± 0.09	4.40 ± 0.28	0.073
65°–70°	5.67 ± 0.04	528 ± 17	3.94 ± 0.11	5.69 ± 0.34	0.089
70°–75°	5.66 ± 0.03	574 ± 17	4.03 ± 0.15	6.71 ± 0.42	0.085
75°–80°	5.65 ± 0.04	599 ± 20	4.04 ± 0.16	6.44 ± 0.45	0.096
80°–90°	5.37 ± 0.08	706 ± 55	3.97 ± 0.41	6.07 ± 1.11	0.148

coefficients determined by the fitting method. The exponential function was used to describe the density structure at low altitudes (below about 3000 km) by *Kletzing et al.* [1998], while the power law function was used for fitting the electron density profile at high altitudes (>5000 km) by *Persoon et al.* [1983], *Hilgers* [1992], *Nsumei et al.* [2003, 2008], and *Johnson and Wygant* [2003]. The median data are weighted by the number of orbit passes (n_{pass}) in each bin and r^{-3} to correct for the volume of bins.

[15] As a rough indication, a scale height (h) of 383 km [*Kletzing et al.*, 1998] corresponds to 5500 K at an altitude of 1000 km, assuming the plasma mainly consists of O^+ ions. In order to simplify the electron density model, we use equation (3) in different plasma regions of the plasmasphere, trough region, and polar cap. The power law functions were used to describe the field-aligned density profile not only in the polar cap but also in the trough and plasmasphere above 2 R_E [*Goldstein et al.*, 2001; *Denton et al.*, 2002a, 2002b, 2004]. Strictly speaking, the power law function may not be applicable or justified in the plasmasphere, where the field lines are closed and the type of upward field-aligned plasma flow proposed by *Persoon et al.* [1983] do not occur. However, the focus of the present paper is on the electron density distributions in the polar region, and it is beyond our scope to search for the best function for the field-aligned electron density profiles in the plasmasphere: detailed analyses of the plasmasphere are performed by T. Ikeda et al. (manuscript in preparation, 2009).

[16] In order to estimate the fitting accuracy, ε is defined as,

$$\varepsilon = \sqrt{\frac{\sum\left((\log_{10} N_{\mathrm{e\_model}} - \log_{10} N_{\mathrm{e\_median}})^2 n_{\mathrm{pass}} r^{-3}\right)}{\sum\left(n_{\mathrm{pass}} r^{-3}\right)}}, \qquad (4)$$

where $N_{\mathrm{e\_median}}$ and $N_{\mathrm{e\_model}}$ are the median electron density and the electron density calculated from the model equation (3), respectively.

[17] The representative latitude of each ILAT bin was defined at its center ILAT except for the highest ILAT ("≥80°") bin, where the representative latitude was defined as 82.5°. The electron densities calculated by the fitting method were interpolated using exponential functions in the ILAT direction. Then, the meridional electron density distribution models in each season were obtained. The distributions above 88° ILAT were not plotted due to the limitation of the orbital coverage.

[18] The dependence on SZA at the magnetic footprint was analyzed in the region of ILAT ≥ 70° in the nightside. The magnetic footprints at 120 km altitude were calculated using the IGRF-10 model.

3. Result

[19] First, we analyze the seasonal variation of field-aligned electron density profiles. Figures 2a–2c show profiles of median and fitted electron densities in the nightside polar cap in an ILAT range of 75°–80° in the summer, equinox, and winter seasons, respectively. Error bars indicate quartiles, which show 25% deviations of the data on either side of the medians. It is impossible to calculate standard deviations, since the electron density cannot be derived in the case where f_{pe} is lower than 20 kHz. In the cases where less than 25% of the data are "below 5.5 /cc," the lower quartiles are not affected by the existence of the data "below 5.5 /cc." In the cases where more than 25% of the data are "below 5.5 /cc," the lower quartiles are regarded as 5.5 /cc, which is the lower limit of the electron density shown in Figure 2. In the cases where more than half of the data fall below 5.5 /cc, the medians and error bars are not plotted, since the bins are ignored in obtaining the empirical models. The coefficients in equation (3), root-mean-square errors of the coefficients, and ε in equation (4) are determined as listed in Tables 1–6. The number of orbit passes filling each bin is shown in Figures 4b, 4d, and 4f. As shown in Figure 2, the electron density profiles at low altitudes are well fitted by exponential functions, while the profiles at high altitudes are well described by power law functions. The scale height (h) shows a seasonal variation and is largest in the summer (501 km) and smallest in the winter (185 km). The scale height in equinox is intermediate (412 km) between that in the summer and in the winter. The transition height, where the power law term equals to the exponential term, is largest in the summer (4000 km) and smallest in the winter (1500 km); this is caused by the larger scale height in the summer than that in the winter. The largest seasonal variation is identified at 1700 km altitude where the electron densities in the summer and winter are 2.8×10^4 and 5.2×10^2 /cc, respectively. Thus the summer-to-winter electron density ratio is up to about 50. In comparison, the seasonal variation at high altitudes is smaller; the electron densities in the summer and winter are 44 and 7.9 /cc, respectively, at 8000 km altitude. This corresponds to an electron density ratio of 5.6. The power indices (α) are derived as 5.84–7.37. Following the discussions in section 1 and in the work of *Persoon et al.* [1983], the indices imply that the upward flow velocity of the plasma increases in proportion to $r^{2.84-4.37}$ above the transition heights.

[20] Figures 2d–2f show electron density profiles in the dayside in the same ILAT range as Figures 2a–2c. This ILAT region corresponds to the averaged location of the cusp when the interplanetary magnetic field B_z is larger than −2 nT [*Newell et al.*, 2006]. The scale heights derived in this region in the summer, equinox, and winter seasons are 599, 442, and 276 km, respectively. The scale height is largest in the summer and smallest in the winter. The

Table 2. Coefficients, Root-Mean-Square Errors of the Coefficients, and ε in the Summer in the Nightside

Invariant Latitude	$\log_{10}(n_1$ (/cc))	h (km)	$\log_{10}(n_2$ (/cc))	α	ε
45°–50°	6.05 ± 0.06	329 ± 12	3.92 ± 0.03	1.50 ± 0.08	0.048
50°–55°	6.02 ± 0.06	345 ± 15	3.58 ± 0.04	1.09 ± 0.11	0.074
55°–60°	5.82 ± 0.07	441 ± 23	3.38 ± 0.08	1.57 ± 0.24	0.126
60°–65°	5.84 ± 0.06	449 ± 19	3.70 ± 0.08	4.27 ± 0.23	0.103
65°–70°	5.74 ± 0.05	518 ± 14	3.89 ± 0.10	6.45 ± 0.27	0.076
70°–75°	5.76 ± 0.04	513 ± 10	3.94 ± 0.06	6.70 ± 0.15	0.041
75°–80°	5.91 ± 0.06	501 ± 13	3.70 ± 0.06	5.84 ± 0.16	0.041
80°–90°	5.62 ± 0.09	592 ± 20	3.28 ± 0.09	4.63 ± 0.25	0.044

Table 4. Coefficients, Root-Mean-Square Errors of the Coefficients, and ε in the Equinox in the Nightside

Invariant Latitude	$\log_{10}(n_1$ (/cc))	h (km)	$\log_{10}(n_2$ (/cc))	α	ε
45°–50°	6.16 ± 0.07	242 ± 13	3.86 ± 0.05	1.49 ± 0.20	0.099
50°–55°	6.25 ± 0.10	163 ± 10	3.79 ± 0.04	2.14 ± 0.18	0.108
55°–60°	6.12 ± 0.11	166 ± 11	3.76 ± 0.05	3.40 ± 0.18	0.127
60°–65°	5.22 ± 0.08	418 ± 28	3.30 ± 0.13	3.47 ± 0.47	0.176
65°–70°	5.38 ± 0.08	383 ± 29	4.10 ± 0.11	7.59 ± 0.40	0.144
70°–75°	5.24 ± 0.07	459 ± 31	4.25 ± 0.11	7.94 ± 0.38	0.101
75°–80°	5.54 ± 0.07	412 ± 25	4.16 ± 0.11	7.37 ± 0.39	0.141
80°–90°	5.68 ± 0.07	399 ± 20	4.10 ± 0.09	7.01 ± 0.30	0.125

transition height is also largest in the summer (4200 km) and smallest in the winter (1800 km). The same trend has already been identified in the nightside (Figures 2a–2c). Although the medians in the winter have larger scatters due to the small number of orbit passes in each bin (less than 10 orbit passes in the bins between 3500 and 8400 km; see Figure 4f), the maximum summer-to-winter electron density ratio (9.6×10^3 /cc/7.3×10^2 /cc) is about 13 at 2400 km altitude. This ratio is attributed to the large seasonal variation of the scale height as well as that of the transition height. In comparison, the corresponding ratio at 8000 km altitude (59 /cc/13 /cc) is 4.5. At both altitudes, the density ratio is smaller than that in the nightside.

[21] Comparing the electron density profiles in the dayside (Figures 2a–2c) to those in the nightside (Figures 2d–2f), the scale height in the dayside is larger than that in the nightside in each season. In the winter, the electron density ratio of the dayside and nightside is up to 5 at 1500 km altitude. In the summer and equinox, the day-night asymmetries are a factor of <2 which are smaller than that in the winter. A comparison with the large seasonal variation of a factor of 13–50 leads us to conclude that seasonal variation affects the electron density more strongly than the day-night asymmetry does.

[22] Figures 2g–2i show the electron density profiles in the dayside in the ILAT range of 70°–75°. This ILAT region corresponds to the statistical dayside ionospheric trough [*Shestakova et al.*, 1997]. The scale heights are 574, 439, and 255 km, in the summer, equinox, and winter seasons, respectively. The scale height is largest in the summer and smallest in the winter. The transition height is also largest in the summer (4100 km) and smallest in the winter (2300 km). The maximum summer-to-winter electron density ratio (7.1×10^3 /cc/1.5×10^2 /cc) is 47 at 2500 km altitude. This ratio is larger than that at 75°–80° ILAT shown in Figures 2d–2f. In comparison, the corresponding ratio (46 /cc/13 /cc) at 8000 km altitude is smaller (3.5), and this trend is similar to that at 75°–80° ILAT.

[23] Next, we analyzed the latitudinal dependence of the electron density distributions. Figures 3a–3c show latitudinal dependences of the electron density distributions in the dayside in the summer, equinox, and winter seasons, respectively. Figures 3d–3f show those in the nightside. The electron densities at each altitude and ILAT were calculated from equation (3) with coefficients determined by the fitting method. The ILAT dependences of electron densities in each season are small (within a factor of 2) above 75° in the dayside and above 70° ILAT in the nightside. The day-night asymmetries above 75° ILAT are within a factor of 5, which are consistent with the results by *Johnson et al.* [2001].

[24] The electron density at 1000 km altitude has a minimum near 60° ILAT in the nightside in the equinox and in both the dayside and nightside in the winter. This latitude is close to the statistical main trough latitude from the premidnight to the morning sector [*Shestakova et al.*, 1997; *Werner and Prölss*, 1997; *Liu et al.*, 2007]. These results are consistent with the tendency that the ionospheric trough is deeper in the winter (dark) than in the summer (sunlit) [*Nishida*, 1967; *Grebowsky et al.*, 1976; *Yizengaw et al.*, 2005]. However, the location of the main trough latitude is largely dependent on MLT (~67° at 18 hours, ~58° at 3 hours, ~60° at 7 hours) [*Shestakova et al.*, 1997; *Werner and Prölss*, 1997]. In order to identify the detailed character of this dependence much more data are required, and this should be studied in the future. However, within the present

Table 3. Coefficients, Root-Mean-Square Errors of the Coefficients, and ε in the Equinox in the Dayside

Invariant Latitude	$\log_{10}(n_1$ (/cc))	h (km)	$\log_{10}(n_2$ (/cc))	α	ε
45°–50°	5.52 ± 0.08	466 ± 26	3.77 ± 0.04	0.94 ± 0.12	0.051
50°–55°	5.21 ± 0.05	605 ± 25	3.45 ± 0.04	0.71 ± 0.11	0.045
55°–60°	5.27 ± 0.05	575 ± 20	3.19 ± 0.05	1.12 ± 0.15	0.058
60°–65°	5.82 ± 0.16	335 ± 31	3.80 ± 0.08	4.74 ± 0.27	0.159
65°–70°	5.45 ± 0.05	473 ± 14	3.42 ± 0.08	4.59 ± 0.23	0.081
70°–75°	5.50 ± 0.06	439 ± 18	3.66 ± 0.09	6.06 ± 0.28	0.113
75°–80°	5.65 ± 0.07	442 ± 22	4.12 ± 0.10	6.95 ± 0.29	0.117
80°–90°	5.86 ± 0.07	342 ± 14	3.94 ± 0.05	5.92 ± 0.16	0.089

Table 5. Coefficients, Root-Mean-Square Errors of the Coefficients, and ε in the Winter in the Dayside

Invariant Latitude	$\log_{10}(n_1$ (/cc))	h (km)	$\log_{10}(n_2$ (/cc))	α	ε
45°–50°	5.60 ± 0.06	388 ± 18	3.70 ± 0.05	0.95 ± 0.19	0.069
50°–55°	5.73 ± 0.06	337 ± 15	3.63 ± 0.05	1.51 ± 0.17	0.094
55°–60°	6.10 ± 0.09	189 ± 11	3.82 ± 0.04	3.10 ± 0.16	0.117
60°–65°	6.18 ± 0.14	168 ± 13	3.84 ± 0.06	5.25 ± 0.25	0.174
65°–70°	5.93 ± 0.04	242 ± 5	2.59 ± 0.08	2.83 ± 0.27	0.108
70°–75°	5.94 ± 0.06	255 ± 8	2.63 ± 0.12	4.31 ± 0.39	0.169
75°–80°	5.90 ± 0.11	276 ± 20	3.86 ± 0.15	7.83 ± 0.58	0.235
80°–90°	5.84 ± 0.13	262 ± 25	4.03 ± 0.13	7.95 ± 0.46	0.215

Table 6. Coefficients, Root-Mean-Square Errors of the Coefficients, and ε in the Winter in the Nightside

Invariant Latitude	$\log_{10}$ (n_1 (/cc))	h (km)	$\log_{10}(n_2$ (/cc))	α	ε
45°–50°	4.33 ± 0.07	812 ± 117	3.50 ± 0.08	0.23 ± 0.24	0.073
50°–55°	4.81 ± 0.11	386 ± 42	3.56 ± 0.04	1.07 ± 0.13	0.077
55°–60°	5.44 ± 0.10	221 ± 13	3.22 ± 0.03	1.32 ± 0.11	0.080
60°–65°	5.62 ± 0.16	186 ± 16	3.02 ± 0.06	3.40 ± 0.21	0.168
65°–70°	5.93 ± 0.16	176 ± 14	3.01 ± 0.07	5.39 ± 0.23	0.180
70°–75°	5.89 ± 0.16	218 ± 18	3.18 ± 0.09	6.41 ± 0.29	0.195
75°–80°	6.13 ± 0.13	185 ± 12	3.28 ± 0.06	6.76 ± 0.21	0.147
80°–90°	5.77 ± 0.11	244 ± 15	3.29 ± 0.11	7.02 ± 0.40	0.166

analysis, the density minimum appeared above 2000 km altitude in the dayside in the winter is consistent with the observation result on the Cosmos-900 satellite in the dayside trough at the ionosphere [*Shestakova et al.*, 1997].

[25] Figures 4a, 4c, and 4e show the meridional electron density distributions in the altitude range of 1000–10,500 km in the summer, equinox, and winter seasons, respectively. The electron density distributions are derived from fitted field-aligned profiles using equation (3). Figures 4b, 4d, and 4f indicate the number of orbit passes in each bin. The coefficients, the root-mean-square errors of the coefficients, and ε are listed in Tables 1–6. The density distributions below 1000 km altitude are not shown in Figures 4a, 4c, and 4e, since several ILAT bins have only a few orbit passes below this altitude and the densities in these bins are from extrapolations. The electron density has a steep gradient in ILAT near 65° ILAT above about 5000 km altitude. This corresponds to the plasmapause. Since the electron density is lower in the winter (nightside) than in the summer (dayside) in the polar region, the plasmapause can be seen down to lower altitudes in the winter (nightside) than in the summer (dayside). The density minimum in the 70°–75° ILAT bin in the dayside is clearly seen in the winter. Figure 5 shows the summer-to-winter electron density ratio. The seasonal variation of the electron density shows a maximum summer-to-winter electron density ratio of 10–50 near 2000 km altitude in the trough and polar regions. The maximum ratio is smaller in the dayside polar cap region compared to that in the trough and nightside polar regions. On the other hand, the seasonal variation of the electron density in the high altitude trough and polar regions above about 5000 km altitude is relatively small (about a factor of 5). The electron density in a region of ILAT below 60° (plasmasphere) also shows a small seasonal variation with a factor of less than 2 above 3000 km altitude.

[26] Last, we analyze the SZA dependence of the field-aligned electron density profile. Figures 6a–6d shows the SZA dependence of profiles of medians and fitted curves for different ranges of SZA in a region of ILAT $\geq$ 70° in the nightside; all data were used without seasonal classifications. This region is chosen for analysis, since the ILAT dependences are small in each season as shown in Figures 3d–3f. The scale heights in SZA ranges of 60°–80°, 80°–100°, 100°–120°, and 120°–140° are derived as 551, 432, 301, and 213 km, respectively. As the SZA is smaller, the scale height is larger. The scale height in a SZA range of 60°–80° is a factor of 2.6 larger than that in a SZA range of 120°–140°. The transition height in SZA ranges of 60°–80° (3900 km), 80°–100° (2300 km), 100°–120° (1800 km), and 120°–140° (1600 km) decreases with increasing SZA. The power indices are derived as 6.57–8.25. The indices imply that the upward flow velocity of the plasma increases in proportion to $r^{3.57-5.25}$ above the transition heights. Comparing the electron densities in SZA ranges of 60°–80° (1.7×10^4 /cc) and 120°–140° (3.2×10^2 /cc), the largest SZA dependence is identified at 1900 km altitude, with a factor of 51. Above about 5000 km, the SZA dependence of the electron density is within a factor of 10. The large SZA dependence at lower altitudes strongly suggests that photoionization processes in the ionosphere strongly control the electron density up to at least an altitude of about 5000 km in the nightside polar region.

4. Discussion

4.1. Comparison to Other Empirical Models

[27] Figure 7 shows the comparison of the electron density profiles derived by Akebono to empirical models based on other satellite observations. Figures 7a and 7b show the profiles obtained in sunlit and dark conditions, respectively. Figure 7c shows the monthly mean $F_{10.7}$ solar radio flux index (thin red line), and periods covered by each satellite data set discussed below. The red curves in Figures 7a and 7b correspond to the electron density profiles in Figure 6a (SZA 60°–80°) and Figure 6d (SZA 120°–140°), respectively. Empirical models based on the DE-1 [*Persoon et al.*, 1983] (gray), Viking [*Hilgers*, 1992] (black), S3–3 [*Kletzing et al.*, 1998] (orange) observations, and Global Core Plasma Model (GCPM) [*Gallagher et al.*, 2000] (pink) were created from density data without concerning geomagnetic and SZA effects. *Kletzing et al.* [1998] derived two profiles based on the S3–3 observations in a region of ILAT > 80° for all MLT, and a region of ILAT 65°–80° for the premidnight sector (1800–2400 MLT). The former is shown in Figure 7a and the latter is shown in Figure 7b. For the electron density profiles based on the DE-1, Viking observations, and GCPM, the same profiles are shown in both Figures 7a and 7b. Electron density models based on the Polar observations [*Johnson and Wygant*, 2003] (green) were derived from data during geomagnetically quiet periods ($Kp \leq 2$). The profiles obtained from the data at SZA lower than 70° and at SZA higher than 110° are shown in Figures 7a and 7b, respectively. Electron density profiles based on the IMAGE observations [*Nsumei et al.*, 2008] (blue) are plotted for $Kp = 0$ and SZA = 70° (Figure 7a) and SZA = 130° (Figure 7b).

[28] As shown in Figure 7a, the density profile in sunlit conditions above 4800 km altitude on Akebono agrees well with the profiles based on IMAGE and Polar observations. Below 4000 km altitude in sunlit conditions, the electron density model based on the IMAGE observations is slightly (a factor of <3) lower than that based on the Akebono observations. As noted earlier, the electron density profiles based on DE-1 and GCPM include data both in sunlit and dark conditions. Although comparison between these profiles and the Akebono profiles is not straightforward, the DE-1 and GCPM profiles lie between the Akebono profiles in sunlit and dark conditions as shown in Figures 7a and 7b.

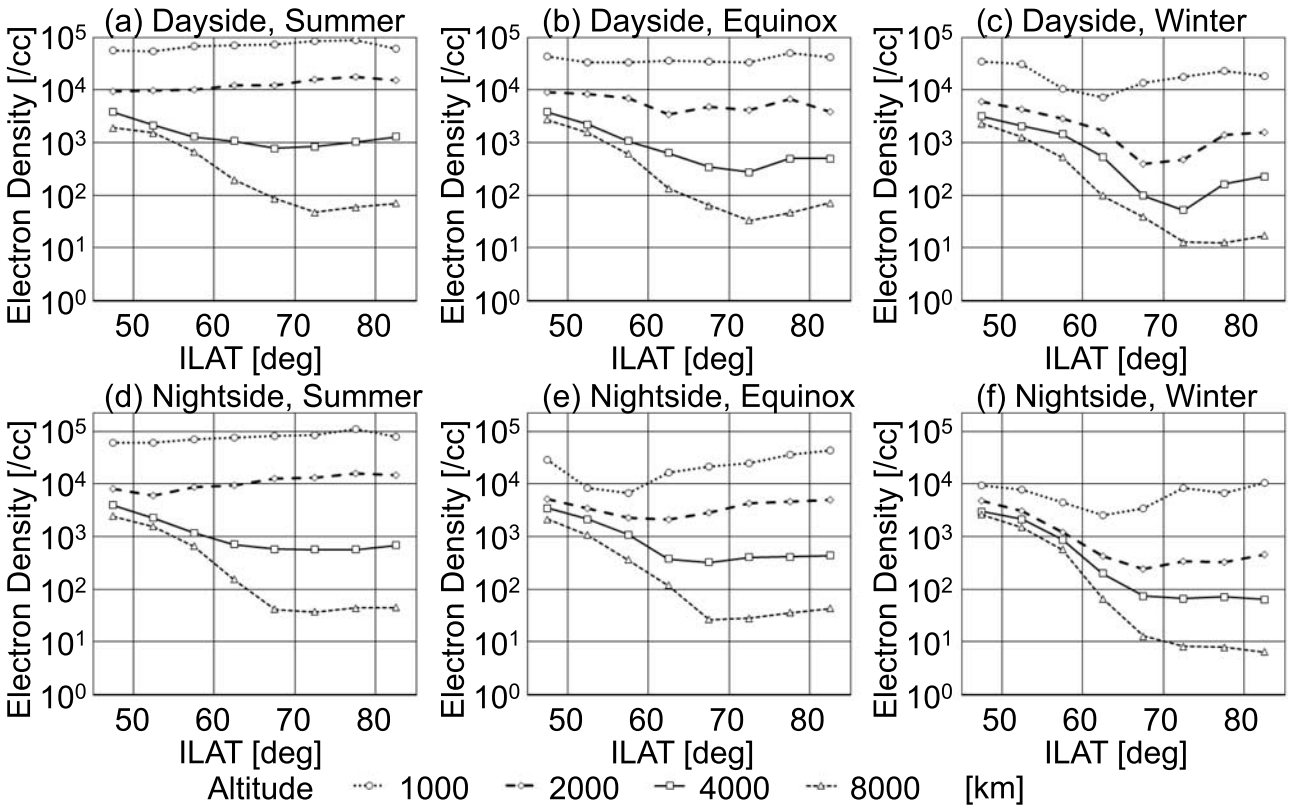

Figure 3. ILAT dependences of electron density distributions. (a–c) Electron density distributions in the dayside in the summer, equinox, and winter seasons, respectively. (d–f) Those in the nightside. The electron densities at each altitude and ILAT are calculated from the fitted field-aligned profiles.

Since the electron density profiles based on the Viking and S3–3 observations also contain both in sunlit and dark conditions, comparison between these profiles and the Akebono profiles is not straightforward. However, the Viking and S3–3 profiles were lower than the middle of the Akebono profiles in dark and sunlit conditions as presented in Figures 7a and 7b. It is probably due to the solar cycle dependence of the electron density: the Akebono data used in the present study were obtained near solar maximum, while the Viking and S3–3 observations covered near solar minimum (Figure 7c). Note that although the S3–3 data were obtained in the period from solar minimum to solar maximum (Figure 7c), the majority of the data were obtained early in the period. In Figure 7b, the electron density profile based on the IMAGE observations is a factor of 2–3 larger than that based on the Akebono observations. Although the electron density profile in dark conditions based on the Polar observations was obtained near solar maximum (Figure 7c), it is about one order lower than other profiles. The electron density obtained by the Polar satellite is derived from the spacecraft potential, using an empirical relation between the spacecraft potential and electron density obtained near solar minimum [*Scudder et al.*, 2000]. Using the Cluster satellites, *Pedersen et al.* [2008] showed that stronger solar extreme ultraviolet and X-ray radiations near solar maximum increase currents of photoelectrons escaping from probes and the satellite body compared to the case near solar minimum and alter the empirical relation between the spacecraft potential and electron density. This effect causes underestimation of the electron density, when the empirical relation between the spacecraft potential and electron density obtained near solar minimum is used near solar maximum. This may contribute to the difference between Polar and other profiles.

[29] It has been reported that the density gradient along the magnetic field is steeper in sunlit conditions or summer than that in dark conditions or winter between 1.75 and 5 R_E [*Laakso et al.*, 2002; *Johnson and Wygant*, 2003; *Nsumei et al.*, 2008]. In the present study, the power index above the transition height does not show a distinct change in season or SZA. This is probably because the coefficients in the power law term in the present study in equation (3) are determined by the data in a narrower altitude range (<2.6 R_E) than those in the studies by *Laakso et al.* [2002], *Johnson and Wygant* [2003], and *Nsumei et al.* [2008] (about 1.5–5 R_E). If the altitude range is extended to higher altitudes, the power index may change, and the seasonal dependence may be clearer.

4.2. Comparison to Theoretical Models and Simulations

[30] Plasma density distributions have been investigated not only by observations but also by one-dimensional theoretical models [e.g., *Ganguli et al.*, 1987; *Cannata and Gombosi*, 1989; *Tam et al.*, 1995, 1998] and three-dimensional models [e.g., *Schunk and Sojka*, 1989, 1997; *Demars and Schunk*, 2001]. Here we compare the plasma density distributions for the geomagnetically quiet periods

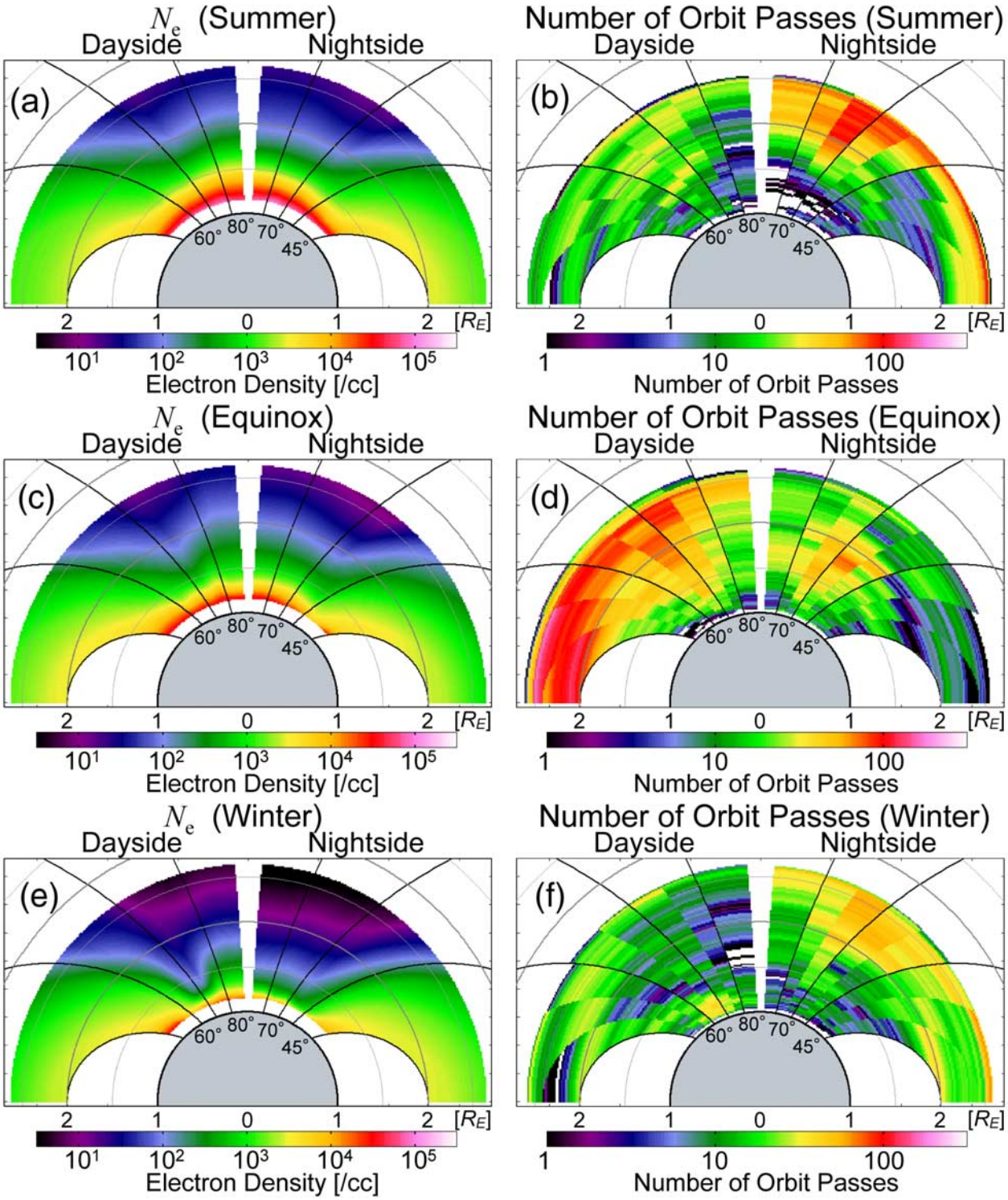

Figure 4. Electron density distribution models in a region of ILAT $\geq 45°$ in an altitude range of 1000–10,500 km. Meridional electron density distribution models fitted by the functions described in equation (3) in the (a) summer, (c) equinox, and (e) winter seasons. The number of orbit passes in each bin are shown in the (b) summer, (d) equinox, and (f) winter seasons. The dipole magnetic field lines at ILAT of 45°, 60°, 70° and 80° are shown in each panel.

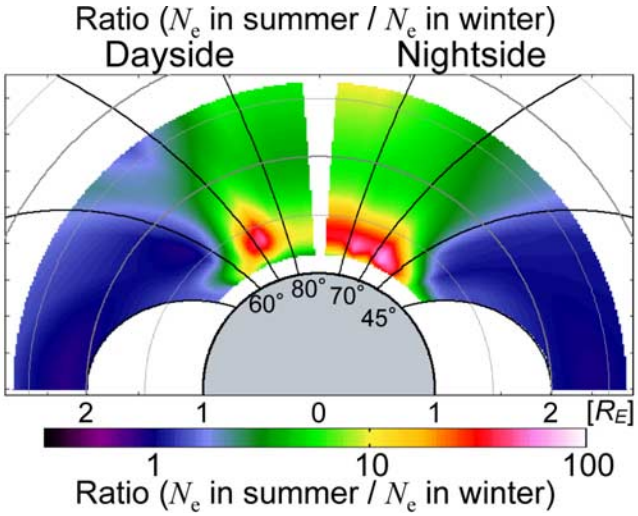

Figure 5. The distribution of the summer-to-winter electron density ratio. The format is the same as Figure 4.

derived in the present study to some of these models. *Cannata and Gombosi* [1989] proposed a one-dimensional polar wind model in an altitude range of 200–4000 km, using a condition of local noon in summer with $F_{10.7} = 180$. The sum of the density of H^+ and O^+ given by the model agrees well with the present Akebono result within a factor of 3. *Tam et al.* [1998] developed a self-consistent model of the one-dimensional polar wind driven by photoelectrons in an altitude range of 500–12,800 km. They performed four cases of the number density ratio of photoelectrons and thermal electrons. The sum of the density of H^+ and O^+ given by the model is almost the same as the electron density based on the Akebono observations near an altitude of 3000 km, while the density given by the model is about two orders greater than that based on the Akebono observations near an altitude of 10,000 km. The model tends to overestimate ion and electron temperatures and O^+ field-aligned velocities at an altitude of about 1000 km than the observations in the polar cap [*Loranc et al.*, 1991; *Abe et al.*, 1993a]. Since the density gradient of the model at low altitudes is more gradual than that derived in the present study, the electron density at high altitudes is overestimated.

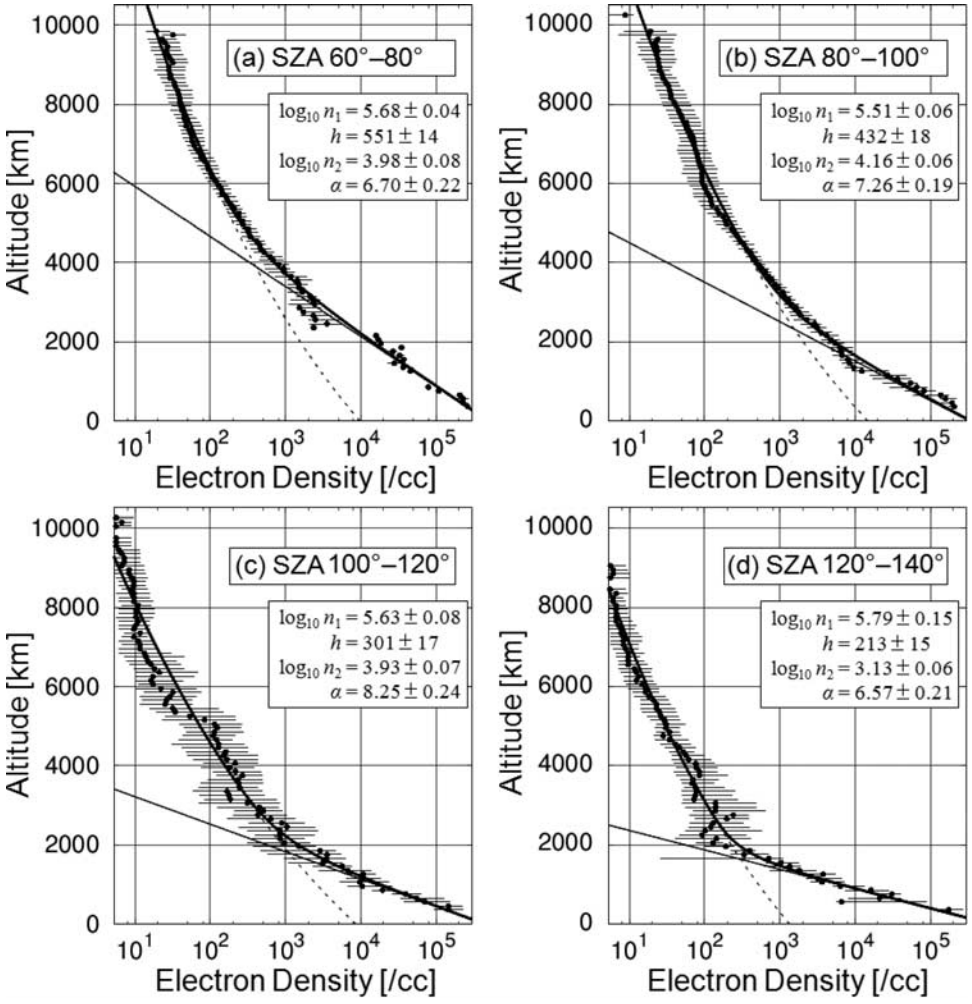

Figure 6. Profiles of median and fitted electron densities in every 20° SZA bin, using all the data without seasonal classifications in a region of ILAT $\geq$ 70° in the nightside. The format is the same as Figure 2.

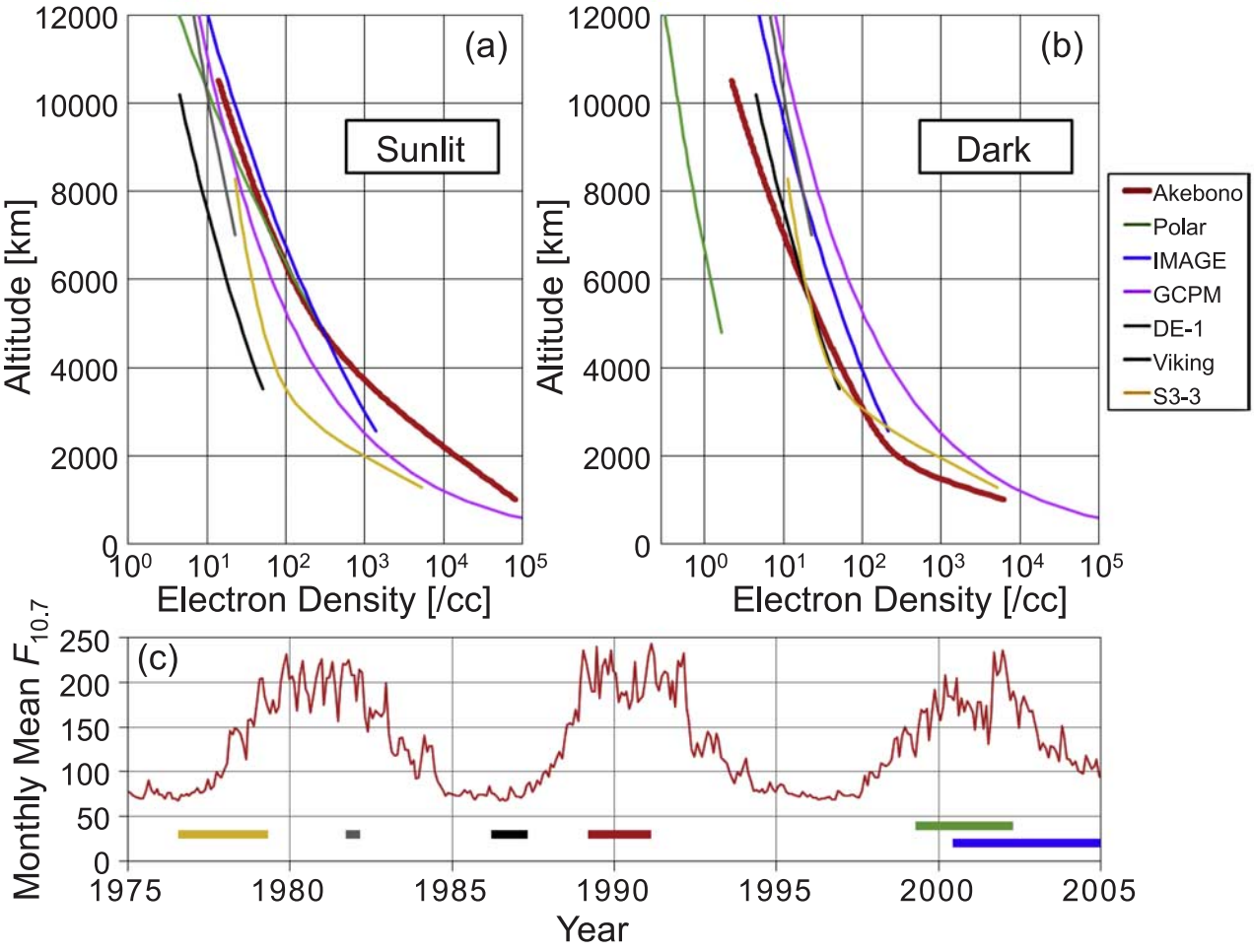

Figure 7. Comparison of the electron density profiles derived in the present study to empirical models proposed using other satellite observations in (a) sunlit and (b) dark conditions. Note that the same profiles are shown in both Figures 7a and 7b for DE-1, GCPM, and Viking, since these profiles were obtained without any consideration of SZA effects. The profile based on S3–3 without any consideration of SZA effects in a region of ILAT > 80° for all MLT is shown in Figure 7a, and that in a region of ILAT 65°–80° for the premidnight sector (1800–2400 MLT) is shown in Figure 7b. (c) The phase of the solar cycle of each data set. The thin red line denotes the monthly mean $F_{10.7}$ solar radio flux index. Thick lines indicate periods covered by each data set.

[31] *Demars and Schunk* [2001] performed a simulation of the polar wind using a time-dependent, three-dimensional, fluid model. The sum of the density of H^+ and O^+ given by the simulation ($\sim 10^3$ /cc) during geomagnetically quiet periods (Kp = 1) at an altitude of 2000 km at solar maximum ($F_{10.7}$ = 210) winter solstice agrees well with the electron density based on the Akebono observations ($\sim 10^3$ /cc) in the winter in the polar region. At an altitude of 500 km, the density given by the simulation ($\sim 2 \times 10^5$ /cc) also agrees well with the electron density based on the Akebono observations ($\sim 2 \times 10^5$ /cc) shown in Figures 2c, 2f, and 2i. Sufficient data of Akebono exist at this altitude in the winter as shown in Figure 4f, although the electron density model derived in this study does not extend to below 1000 km altitude. On the other hand, the sum of H^+ and O^+ densities given by the simulation ($\sim 2 \times 10^3$ /cc) at 2000 km altitude during geomagnetically quiet periods at solar maximum summer solstice is about one order less than the electron density based on the Akebono observations ($\sim 2 \times 10^4$ /cc) in the summer in the polar region. In contrast, the density given by the simulation ($\sim 10^6$ /cc) at 500 km altitude is greater than that obtained by Akebono in the summer ($\sim 3 \times 10^5$ /cc), as shown in Figures 2a, 2d, and 2g, although rather few data samples exist near this altitude in the summer as shown in Figure 4b. Therefore, it is probable that the density gradient at summer solstice is underestimated in the simulation study. In order to investigate the difference between the observations and simulations, it is important to clarify the temperature and velocity distributions of ions and electrons in future works.

4.3. Formation Mechanisms of the Electron Density Transition

[32] In the present study, a transition of the electron density profile is identified in an altitude range of 1400–4700 km in a region of ILAT ≥ 70°. The transition height is higher in sunlit conditions or summer than in dark con-

ditions or winter. This altitude range is close to the transition altitude region of the electron density profile (1.55–2.0 R_E) pointed out by *Persoon et al.* [1983]. They suggested that the transition is due to the change from a collision-dominated to collisionless regime, a transition in the ion composition of the plasma, or a transition in the plasma flow velocity and plasma temperature. Observations and simulations show that O^+ is dominant in the plasma up to 4000 km altitude [*Chandler et al.*, 1991], and O^+ and H^+ densities are of the same order above about 5000 km altitude [*Watanabe et al.*, 1992; *Su et al.*, 1998; *Barakat and Schunk*, 2006]. This ion composition change can form the transition.

[33] A transition in the plasma flow velocity could form the electron density transition. The upward velocity of O^+ begins to increase above an altitude of 4500–5000 km in the dayside or sunlit conditions [*Abe et al.*, 1993b, 2004], and the altitude is near the transition height identified in the present study in summer or sunlit conditions. Therefore, the variation of the plasma flow velocity may also be related to the transition in sunlit conditions or the dayside. In contrast, since the upward velocity of O^+ does not significantly change in the nightside or dark conditions in the polar cap near the transition height identified in the present study (1400–4700 km) [*Abe et al.*, 1993b, 2004], the variation of the plasma flow velocity is probably not related to the transition in dark conditions or the nightside. Detailed observations of seasonal and SZA dependences of ion composition and plasma velocity are necessary to clarify the formation mechanism of the electron density transition.

4.4. Influence on Auroral Phenomena

[34] Auroral plasma cavities [e.g., *Benson and Calvert*, 1979; *Calvert*, 1981; *Persoon et al.*, 1988; *Janhunen et al.*, 2002] are not clearly seen in Figures 3 and 4. This is due to our analysis method, which uses the median electron density and large bin size in ILAT and MLT. The analyses using the median strongly exclude the small scale structures. Therefore, these density distributions probably represent the density outside cavities or before the formation of cavities during substorms.

[35] Auroral particle acceleration and AKR have seasonal and SZA dependences, indicating that these are more active in the winter or dark conditions than in the summer or sunlit conditions [*Newell et al.*, 1996; *Kasaba et al.*, 1997; *Kumamoto and Oya*, 1998; *Collin et al.*, 1998; *Liou et al.*, 2001; *Morooka and Mukai*, 2003; *Cattell et al.*, 2006]. Observations of upflowing ions and the maximum frequency of AKR showed that lower altitude limit of the auroral acceleration region was located at about 5000 km in the summer and decreased to about 3000 km in the winter [*Kumamoto et al.*, 2001, 2003; *Morooka and Mukai*, 2003; *Green et al.*, 2004]. The result of the present study revealed that there were large (a factor of 5–20) seasonal and SZA dependences of the electron density in this altitude range. This large density variation is expected to strongly affect the formation of the auroral acceleration region.

5. Summary and Conclusion

[36] Seasonal variations of meridional electron density distributions have been investigated, using 2 years of electron density data derived from the plasma wave observations obtained by the Akebono satellite in an altitude range of 300–10,500 km and in a region of ILAT $\geq$ 45° during geomagnetically quiet periods near solar maximum. Electron density profiles at low altitudes are well fitted by exponential functions, while the profiles at higher altitudes are well described by power law functions. A transition of the density profile is identified in an altitude range of 1400–4700 km (ILAT $\geq$ 70°).

[37] The scale height shows a remarkable seasonal variation; the scale height is largest in the summer (~550 km) and smallest in the winter (~250 km) in a region of ILAT $\geq$ 70°. This leads a seasonal variation in which the transition height is highest in the summer (~4000 km) and lowest in the winter (~1800 km). The maximum electron density ratio of 10–50 between summer (~10^4 /cc) and winter (~10^3 /cc) occurs near 2000 km altitude in the trough and polar regions. This maximum ratio is smaller in the dayside polar cap than that in the dayside trough and nightside polar regions. The seasonal variation is smaller (about a factor of 5) above about 5000 km altitude in the trough and polar regions. The seasonal variation is also small (within a factor of 2) in a region of ILAT < 60° (plasmasphere) above 3000 km altitude.

[38] The magnitude of day-night asymmetry in the electron density distributions in each season is smaller than that of the seasonal variation. The scale height is larger in the dayside than that in the nightside in each season. The day-night asymmetries are less than a factor of 2 in the summer and equinox seasons. The day-night asymmetry of the electron density is up to a factor of 5 in the winter. It is concluded that the seasonal variation affects the electron density more strongly than the day-night asymmetry does.

[39] The SZA dependence of the electron density profile in the nightside polar region (ILAT $\geq$ 70°) is derived. The scale height in the SZA range of 60°–80° (549 km) is 2.6 times larger than that in the range of 120°–140° (213 km). Comparing the density profiles in SZA ranges of 60°–80° (1.7×10^4 /cc) and 120°–140° (3.2×10^2 /cc), the largest SZA dependence with a factor of 51 is identified at 1900 km altitude. Above about 5000 km altitude, the SZA dependence is within a factor of 10. These results indicate that photoionization processes in the ionosphere strongly control electron density distributions up to at least about 5000 km altitude. The meridional electron density distribution models derived in the present study will contribute to investigations of the polar wind, ion outflow, and auroral acceleration.

[40] **Acknowledgments.** The Akebono satellite was established by the Institute of Space and Astronautical Science (ISAS/JAXA). The *SYM-H* and *Kp* indices were provided by WDC-C2 for Geomagnetism. The monthly mean $F_{10.7}$ solar radio flux index was provided by NGDC. This work was supported by the 21st century COE program "Advanced Science and Technology Center for the Dynamic Earth" at the Tohoku University and the Research Fellowship of the Japan Society for the Promotion of Science.

[41] Zuyin Pu thanks Dennis Gallagher and Andrew Yau for their assistance in evaluating this paper.

References

Abe, T., K. I. Oyama, S. Watanabe, and H. Fukunishi (1993a), Characteristic features of electron temperature and density variations in field-aligned current regions, *J. Geophys. Res.*, *98*, 11,257–11,266, doi:10.1029/92JA01970.

Abe, T., B. A. Whalen, A. W. Yau, R. E. Horita, S. Watanabe, and E. Sagawa (1993b), EXOS D (Akebono) suprathermal mass spectrometer observations of the polar wind, *J. Geophys. Res.*, *98*, 11,191–11,203, doi:10.1029/92JA01971.

Abe, T., A. W. Yau, S. Watanabe, M. Yamada, and E. Sagawa (2004), Long-term variation of the polar wind velocity and its implication for the ion acceleration process: Akebono/suprathermal ion mass spectrometer observations, *J. Geophys. Res.*, *109*, A09305, doi:10.1029/2003JA010223.

Adrian, M. L. (2002), The density-potential (N_e-$V_{S/C}$) relation in the high-latitude prenoon ionosphere, *Phys. Plasmas*, *9*, 602–618, doi:10.1063/1.1415423.

Barakat, A. R., and R. W. Schunk (2006), A three-dimensional model of the generalized polar wind, *J. Geophys. Res.*, *111*, A12314, doi:10.1029/2006JA011662.

Benson, R. F., and W. Calvert (1979), ISIS 1 observation at the source of auroral kilometric radiation, *Geophys. Res. Lett.*, *6*, 479–482, doi:10.1029/GL006i006p00479.

Calvert, W. (1981), The auroral plasma cavity, *Geophys. Res. Lett.*, *8*, 919–921, doi:10.1029/GL008i008p00919.

Cannata, R. W., and T. I. Gombosi (1989), Modeling the solar cycle dependence of quiet-time ion upwelling at high geomagnetic latitudes, *Geophys. Res. Lett.*, *16*, 1141–1144, doi:10.1029/GL016i010p01141.

Cattell, C., J. Dombeck, C. Carlson, and J. McFadden (2006), FAST observation of the solar illumination dependence of downgoing auroral electron beams: Relationship to electron energy flux, *J. Geophys. Res.*, *111*, A02201, doi:10.1029/2005JA011337.

Chan, K. L., and L. Colin (1969), Global electron density distributions from topside soundings, *Proc. IEEE*, *57*, 990–1004, doi:10.1109/PROC.1969.7143.

Chandler, M. O., J. H. Waite Jr., and T. E. Moore (1991), Observations of polar ion outflows, *J. Geophys. Res.*, *96*, 1421–1428, doi:10.1029/90JA02180.

Collin, H. L., W. K. Peterson, O. W. Lennartsson, and J. F. Drake (1998), The seasonal variation of auroral ion beams, *Geophys. Res. Lett.*, *25*, 4071–4074, doi:10.1029/1998GL900090.

Demars, H. G., and R. W. Schunk (2001), Seasonal and solar cycle variations of the polar wind, *J. Geophys. Res.*, *106*, 8157–8168, doi:10.1029/2000JA000386.

Denton, R. E., J. Goldstein, J. D. Menietti, and S. L. Young (2002a), Magnetospheric electron density model inferred from Polar plasma wave data, *J. Geophys. Res.*, *107*(A11), 1386, doi:10.1029/2001JA009136.

Denton, R. E., J. Goldstein, and J. D. Menietti (2002b), Field line dependence of magnetospheric electron density, *Geophys. Res. Lett.*, *29*(24), 2205, doi:10.1029/2002GL015963.

Denton, R. E., J. D. Menietti, J. Goldstein, S. L. Young, and R. R. Anderson (2004), Electron density in the magnetosphere, *J. Geophys. Res.*, *109*, A09215, doi:10.1029/2003JA010245.

Drakou, E., A. W. Yau, and T. Abe (1997), Ion temperature measurements from the Akebono suprathermal mass spectrometer: Application to the polar wind, *J. Geophys. Res.*, *102*, 17,523–17,539, doi:10.1029/97JA00099.

Fukunishi, H., R. Fujii, S. Kokumun, F. Tohyama, T. Mukai, and H. Oya (1991), Small-scale field-aligned currents observed by the Akebono (EXOS-D) satellite, *Geophys. Res. Lett.*, *18*, 297–300, doi:10.1029/91GL00036.

Gallagher, D. L., P. D. Craven, and R. H. Comfort (2000), Global core plasma model, *J. Geophys. Res.*, *105*, 18,819–18,833, doi:10.1029/1999JA000241.

Ganguli, S. B. (1996), The polar wind, *Rev. Geophys.*, *34*, 311–348, doi:10.1029/96RG00497.

Ganguli, S. B., H. G. Mitchell Jr., and P. L. Palmadesso (1987), Behavior of ionized plasma in the high latitude topside ionosphere: The polar wind, *Planet. Space Sci.*, *35*, 703–713, doi:10.1016/0032-0633(87)90030-4.

Goldstein, J., R. E. Denton, M. K. Hudson, E. G. Miftakhova, S. L. Young, J. D. Menietti, and D. L. Gallagher (2001), Latitudinal density dependence of magnetic field lines inferred from Polar plasma wave data, *J. Geophys. Res.*, *106*, 6195–6201, doi:10.1029/2000JA000068.

Grebowsky, J. M., N. C. Maynard, Y. K. Turunay, and L. J. Lanzerotti (1976), Coincident observations of ionospheric troughs and the equatorial plasmapause, *Planet. Space Sci.*, *24*, 1177–1185, doi:10.1016/0032-0633(76)90154-9.

Grebowsky, J. M., W. R. Hoegy, and T. C. Chen (1990), Solar maximum-minimum extremes in the summer noontime polar cap *F* region ion composition: The measurements, *J. Geophys. Res.*, *95*, 12,269–12,276, doi:10.1029/JA095iA08p12269.

Green, J. L., S. Boardsen, L. Garcia, S. F. Fung, and B. W. Reinish (2004), Seasonal and solar cycle dynamics of the auroral kilometric radiation source region, *J. Geophys. Res.*, *109*, A05223, doi:10.1029/2003JA010311.

Hilgers, A. (1992), The auroral radiating plasma cavities, *Geophys. Res. Lett.*, *19*, 237–240, doi:10.1029/91GL02938.

Janhunen, P., A. Olsson, and H. Laakso (2002), Altitude dependence of plasma density in the auroral zone, *Ann. Geophys.*, *20*, 1743–1750.

Johnson, M. T., and J. R. Wygant (2003), The correlation of plasma density distributions over 5000 km with solar illumination of the ionosphere: Solar cycle and zenith angle observations, *Geophys. Res. Lett.*, *30*(24), 2260, doi:10.1029/2003GL018175.

Johnson, M. T., J. R. Wygant, C. Cattell, F. S. Mozer, M. Temerin, and J. Scudder (2001), Observations of the seasonal dependence of the thermal plasma density in the Southern Hemisphere auroral zone and polar cap at 1 R_E, *J. Geophys. Res.*, *106*, 19,023–19,033, doi:10.1029/2000JA900147.

Kasaba, Y., H. Matsumoto, K. Hashimoto, and R. R. Anderson (1997), The angular distribution of auroral kilometric radiation observed by the GEOTAIL spacecraft, *Geophys. Res. Lett.*, *24*, 2483–2486, doi:10.1029/97GL02599.

Kletzing, C. A., F. S. Mozer, and R. B. Torbert (1998), Electron temperature and density at high latitude, *J. Geophys. Res.*, *103*, 14,837–14,845, doi:10.1029/98JA00962.

Kumamoto, A., and H. Oya (1998), Asymmetry of occurrence-frequency and intensity of AKR between summer polar region and winter polar region sources, *Geophys. Res. Lett.*, *25*, 2369–2372, doi:10.1029/98GL01715.

Kumamoto, A., T. Ono, and H. Oya (2001), Seasonal dependence of the vertical distributions of auroral kilometric radiation sources and auroral particle acceleration regions observed by the Akebono satellite, *Adv. Polar Upper Atmos. Res.*, *15*, 32–42.

Kumamoto, A., T. Ono, and M. Iizima (2003), Seasonal and solar cycle variations of the vertical distribution of the occurrence probability of auroral kilometric radiation sources and of upflowing ion events, *J. Geophys. Res.*, *108*(A1), 1032, doi:10.1029/2002JA009522.

Kumamoto, A., T. Ono, and M. Iizima (2006), Solar zenith angle and solar activity dependences of vertical profile of electron number density in the nightside auroral region, *Adv. Polar Upper Atmos. Res.*, *20*, 27–37.

Laakso, H., and R. Grard (2002), The electron density distribution in the polar cap: Its variability with seasons, and its response to magnetic activity, in *Space Weather Study Using Multipoint Techniques*, edited by L.-H. Lyu, *Proc. COSPAR Colloq.*, *12*, 193–202.

Laakso, H., R. Phaff, and R. Janhunen (2002), Polar observations of electron density distribution in the Earth's magnetosphere. 1. Statistical results, *Ann. Geophys.*, *20*, 1711–1724.

Liou, K., P. T. Newell, and C.-I. Meng (2001), Seasonal effects on auroral particle acceleration and precipitation, *J. Geophys. Res.*, *106*, 5531–5542, doi:10.1029/1999JA000391.

Liu, H., C. Stolle, S. Watanabe, T. Abe, M. Rother, and D. L. Cooke (2007), Evaluation of the IRI model using CHAMP observations in polar and equatorial regions, *Adv. Space Res.*, *39*, 904–909, doi:10.1016/j.asr.2006.08.006.

Lockwood, M., J. H. Waite Jr., T. E. Moore, J. F. E. Johnson, and C. R. Chappell (1985a), A new source of suprathermal O^+ ions near the dayside polar cap boundary, *J. Geophys. Res.*, *90*, 4099–4116, doi:10.1029/JA090iA05p04099.

Lockwood, M., M. O. Chandler, J. L. Horwitz, J. H. Waite Jr., T. E. Moore, and C. R. Chappell (1985b), The cleft ion fountain, *J. Geophys. Res.*, *90*, 9736–9748, doi:10.1029/JA090iA10p09736.

Loranc, M., W. B. Hanson, R. A. Heelis, and J.-P. St.-Maurice (1991), A morphological study of vertical ionospheric flows in the high-latitude *F* region, *J. Geophys. Res.*, *96*, 3627–3646, doi:10.1029/90JA02242.

Lysak, R. L., and W. Lotko (1996), On the kinetic dispersion relation for shear Alfvén waves, *J. Geophys. Res.*, *101*, 5085–5094, doi:10.1029/95JA03712.

Matuura, N., and T. Ondoh (1969), The structure of the topside ionosphere deduced from Alouette data, *Proc. IEEE*, *57*, 1150–1153, doi:10.1109/PROC.1969.7171.

Moore, T. E., M. Lockwood, M. O. Chandler, J. H. Waite Jr., C. R. Chappell, A. Persoon, and M. Sugiura (1986), Upwelling O^+ ion source characteristics, *J. Geophys. Res.*, *91*, 7019–7031, doi:10.1029/JA091iA06p07019.

Morooka, M., and T. Mukai (2003), Density as a controlling factor for seasonal and altitudinal variations of the auroral particle acceleration region, *J. Geophys. Res.*, *108*(A7), 1306, doi:10.1029/2002JA009786.

Nelms, G. L., and G. E. K. Lockwood (1967), Early results from the topside sounder in the Alouette II satellite, *Space Res.*, *7*, 604–623.

Newell, P. T., C.-I. Meng, and K. M. Lyons (1996), Suppression of discrete aurorae by sunlight, *Nature*, *381*, 766–767, doi:10.1038/381766a0.

Newell, P. T., T. Sotirelis, K. Liou, C.-I. Meng, and F. J. Rich (2006), Cusp latitude and optimal solar wind coupling function, *J. Geophys. Res.*, *111*, A09207, doi:10.1029/2006JA011731.

Nishida, A. (1967), Average structure and storm-time change of the polar topside ionosphere at sunspot minimum, *J. Geophys. Res.*, *72*, 6051–6061, doi:10.1029/JZ072i023p06051.

Nsumei, P. A., X. Huang, B. W. Reinisch, P. Song, V. M. Vasyliunas, J. L. Green, S. F. Fung, R. F. Benson, and D. L. Gallagher (2003), Electron density distribution over the northern polar region deduced from IMAGE/radio plasma imager sounding, *J. Geophys. Res.*, *108*(A2), 1078, doi:10.1029/2002JA009616.

Nsumei, P. A., B. W. Reinisch, P. Song, J. Tu, and X. Huang (2008), Polar cap electron density distribution from IMAGE radio plasma imager measurements: Empirical model with the effects of solar illumination and geomagnetic activity, *J. Geophys. Res.*, *113*, A01217, doi:10.1029/2007JA012566.

Oya, H., A. Morioka, K. Kobayashi, M. Iizima, T. Ono, H. Miyaoka, T. Okada, and T. Obara (1990), Plasma wave observation and sounder experiments (PWS) using the Akebono (EXOS-D) satellite–Instrumentation and initial results including discovery of the high altitude equatorial plasma turbulence, *J. Geomagn. Geoelectr.*, *42*, 411–442.

Pedersen, A., et al. (2008), Electron density estimates derived from spacecraft potential measurements on Cluster in tenuous plasma regions, *J. Geophys. Res.*, *113*, A07S33, doi:10.1029/2007JA012636.

Persoon, A. M., D. A. Gurnett, and S. D. Shawhan (1983), Polar cap electron densities from DE 1 plasma wave observations, *J. Geophys. Res.*, *88*, 10,123–10,136, doi:10.1029/JA088iA12p10123.

Persoon, A. M., D. A. Gurnett, W. K. Peterson, J. H. Waite Jr., J. L. Burch, and J. L. Green (1988), Electron density depletions in the nightside auroral zone, *J. Geophys. Res.*, *93*, 1871–1895, doi:10.1029/JA093iA03p01871.

Pollock, C. J., M. O. Chandler, T. E. Moore, J. H. Waite Jr., C. R. Chappell, and D. A. Gurnett (1990), A survey of upwelling ion event characteristics, *J. Geophys. Res.*, *95*, 18,969–18,980, doi:10.1029/JA095iA11p18969.

Schreiber, R., O. Santolik, M. Parrot, F. Lefeuvre, J. Hanasz, M. Brittnacher, and G. Parks (2002), Auroral kilometric radiation source characteristics using ray tracing techniques, *J. Geophys. Res.*, *107*(A11), 1381, doi:10.1029/2001JA009061.

Schunk, R. W., and J. J. Sojka (1989), A three-dimensional time-dependent model of the polar wind, *J. Geophys. Res.*, *94*, 8973–8991, doi:10.1029/JA094iA07p08973.

Schunk, R. W., and J. J. Sojka (1997), Global ionosphere-polar wind system during changing magnetic activity, *J. Geophys. Res.*, *102*, 11,625–11,651, doi:10.1029/97JA00292.

Scudder, J. D., X. Cao, and F. S. Mozer (2000), Photoemission current-spacecraft voltage relation: Key to routine, quantitative low-energy plasma measurements, *J. Geophys. Res.*, *105*, 21,281–21,294, doi:10.1029/1999JA900423.

Shestakova, L. V., A. E. Stepanov, V. L. Khalipov, A. P. Mamrukov, L. D. Filippov, E. K. Zikrach, and V. V. Afonin (1997), High-latitude ionosphere structure in dayside sector on ground-based and satellite measurements, *Adv. Space Res.*, *20*, 415–418, doi:10.1016/S0273-1177(97)00702-3.

Shinbori, A., Y. Nishimura, T. Ono, M. Iizima, A. Kumamoto, and H. Oya (2005), Electrodynamics in the duskside inner magnetosphere and plasmasphere during a super magnetic storm on March 13–15, 1989, *Earth Planets Space*, *57*, 643–659.

Su, Y.-J., J. L. Horwitz, T. E. Moore, B. L. Giles, M. O. Chandler, P. D. Craven, M. Hirahara, and C. J. Pollock (1998), Polar wind survey with the Thermal Ion Dynamics Experiment/Plasma Source Instrument suite aboard POLAR, *J. Geophys. Res.*, *103*, 29,305–29,337, doi:10.1029/98JA02662.

Tam, S. W. Y., F. Yasseen, T. Chang, and S. B. Ganguli (1995), Self-consistent kinetic photoelectron effects on the polar wind, *Geophys. Res. Lett.*, *22*, 2107–2110, doi:10.1029/95GL01846.

Tam, S. W. Y., F. Yasseen, and T. Chang (1998), Further development in theory/data closure of the photoelectron-driven polar wind and day-night transition of the outflow, *Ann. Geophys.*, *16*, 948–968, doi:10.1007/s00585-998-0948-2.

Tu, J.-N., J. L. Horwitz, P. A. Nsumei, P. Song, X.-Q. Huang, and B. W. Reinish (2004), Simulation of polar cap field-aligned electron density profiles measured with the IMAGE radio plasma imager, *J. Geophys. Res.*, *109*, A07206, doi:10.1029/2003JA010310.

Tu, J., P. Song, B. W. Reinish, X. Huang, J. L. Green, H. U. Frey, and P. H. Reiff (2005), Electron density images of the middle- and high-latitude magnetosphere in response to the solar wind, *J. Geophys. Res.*, *110*, A12210, doi:10.1029/2005JA011328.

Tu, J.-N., M. Dahr, P. Song, B. W. Reinisch, J. L. Green, R. F. Benson, and A. J. Coster (2007), Extreme polar cap density enhancement along magnetic field lines during an intense storm, *J. Geophys. Res.*, *112*, A05201, doi:10.1029/2006JA012034.

Watanabe, S., B. A. Whalen, and A. W. Yau (1992), Thermal ion observations of depletion and refilling in the plasmaspheric trough, *J. Geophys. Res.*, *97*, 1081–1096, doi:10.1029/91JA02818.

Werner, S., and G. W. Prölss (1997), The position of the ionospheric trough as a function of local time and magnetic activity, *Adv. Space Res.*, *20*, 1717–1722, doi:10.1016/S0273-1177(97)00578-4.

Xiao, F., L. Chen, H. Zheng, and S. Wang (2007), A parametric ray tracing study of superluminous auroral kilometric radiation wave modes, *J. Geophys. Res.*, *112*, A10214, doi:10.1029/2006JA012178.

Yau, A. W., and M. André (1997), Sources of ion outflow in the high latitude ionosphere, *Space Sci. Rev.*, *80*, 1–25, doi:10.1023/A:1004947203046.

Yau, A. W., T. Abe, and W. K. Peterson (2007), The polar wind: Recent observations, *J. Atmos. Sol. Terr. Phys.*, *69*, 1936–1983, doi:10.1016/j.jastp.2007.08.010.

Yizengaw, E., H. Wei, M. B. Boldwin, D. Galvan, L. Mandrake, A. Manucci, and X. Pi (2005), The correlation between mid-latitude trough and the plasmapause, *Geophys. Res. Lett.*, *32*, L10102, doi:10.1029/2005GL022954.

M. Iizima, Shukutoku Gakuen, 5-14-1 Maenocho, Itabashi-ku, Tokyo, 174-8643, Japan.

N. Kitamura, Y. Nishimura, and T. Ono, Department of Geophysics, Tohoku University, Sendai, 980-8578, Japan. (kitamura@stpp1.geophys.tohoku.ac.jp)

A. Kumamoto, Planetary Plasma and Atmospheric Research Center, Tohoku University, 6-3 Aramaki, Aoba-ku, Sendai, 980-8578, Japan.

A. Shinbori, Solar-Terrestrial Environment Laboratory, Nagoya University, Furoucho, Chikusa-ku, Nagoya, 464-8601, Japan.